Helicity reversion in high-order-harmonic generation driven by bichromatic counter-rotating circularly polarized laser fields

Xiaofan Zhang,[1] Liang Li,[1] Xiaosong Zhu,[1,*] Xi Liu,[1] Qingbin Zhang,[1] Pengfei Lan,[1] and Peixiang Lu[1,2]

[1]*School of Physics, Huazhong University of Science Technology, Wuhan 430074, China*

[2]*Laboratory of Optical Information Technology, Wuhan Institute of Technology, Wuhan 430205, China*

We investigate the polarization properties of high harmonics generated with the bichromatic counter-rotating circularly polarized (BCCP) laser fields by numerically solving the time-dependent Schrödinger equation (TDSE). It is found that the helicity of the elliptically polarized harmonic emission is reversed at particular harmonic orders. Based on the time-frequency analysis and the classical three-step model, the correspondence between the positions of helicity reversions and the classical trajectories of continuum electrons is established. It is shown that the electrons ionized at one lobe of laser field can be divided into different groups based on the different lobes they recombine at, and the harmonics generated by adjacent groups have opposite helicities. Our study performs a detailed analysis of high harmonics in terms of electron trajectories and depicts a clear and intuitive physical picture of the HHG process in BCCP laser fields.

I. INTRODUCTION

High-harmonic generation (HHG) occurs in the interaction of intense femtosecond laser field with atoms or molecules [1,2]. HHG has been intensively studied in experimental and theoretical investigations [3–5], because it promises both applications for generating attosecond pulses [6–8] and for probing the molecular structure [9–12] and ultrafast dynamics [13–17]. The HHG process can be nicely explained by the three-step model [18,19]. First, under the influence of the laser field, an electron escapes from the atom or molecule and reaches the continuum. Then it is accelerated in the laser field. Finally the accelerated electron is driven back to the parent ion and a high energy photon is emitted. According to this picture, only laser fields, which are able to drive the electrons back to the ion, can be used to efficiently generate high harmonics.

Very recently, the bicircualr counter-rotating circularly polarized (BCCP) driving laser field has been a hot spot due to its unique features and applications. A BCCP laser field consists of two coplanar counter-rotating circularly polarized fields with the fundamental field frequency ω and its second harmonic 2ω [20–22]. The time-dependent electric field performs a Lissajous figure on its polarization plane with a threefold symmetry, i.e., it consists of three segments or lobes per cycle. Therefore, the laser field peaks three times one cycle of the fundamental, producing three ionization bursts. The electrons ionized to the continuum near the laser peaks can successfully recombine with the parent ion, radiating an attosecond pulse train with three pulses one cycle of the fundamental [7,23–25].

This attractive laser field has been demonstrated to be an effective tool for fully controlling the high harmonic polarization from linear through elliptical to circular polarization [26]. Importantly, the conversion efficiency for harmonics with arbitrary polarization is comparable to that of the standard HHG process, which yields linearly polarized high harmonics driven by a linearly polarized laser pulse [7,22,26]. When

the BCCP laser pulse is acting on an isotropic medium, in the frequency domain, a comb of high efficiency harmonic with frequency $(3n \pm 1)\omega$ is radiated [7,27–29]. According to the selection rules [26,30–33], the harmonics with frequency $(3n+1)\omega$ have the same helicity as the fundamental while the $(3n-1)\omega$ harmonics have the same helicity as the second harmonic pulse ($3n\omega$ is parity forbidden). Selecting harmonics with one kind of helicity would generate attosecond pulses with circular polarization. Some efforts have been made for the selection, e.g., optimizing the phase-matching conditions [27] or using crossed beams of counter-rotating circularly polarized driving lasers [34]. This circularly polarized light source is very useful for ultrafast spectroscopy, especially for the ultrafast circular dichroism studies [29,35–37]. It was also shown that the bicircular HHG driven by this BCCP laser pulse can be a new method to probe dynamical symmetries of atoms and molecules and their evolution in time [38,39]. These attractive features of HHG in BCCP laser fields are related to the symmetry of the laser field and the corresponding three-step dynamics of the continuum electrons. To better understand the features of HHG in the BCCP laser field, the correspondence between the harmonic polarization and the electron trajectories needs to be established.

In our study, the polarization properties of high harmonics generated in the two-dimensional (2D) model Ne atoms by the BCCP laser fields are investigated. We focus on the helicity reversions in the harmonic spectrum, where the rotation direction of the harmonic electric field reverses at specific orders. To explain this phenomenon, we depict the three-step picture of HHG in BCCP fields and reveal the correspondence between the time-frequency distribution of the harmonic degree of circular polarization and the classical trajectories. Our study helps people better understand the HHG process and depicts a clear picture for the HHG process in the BCCP laser field.

II. THEORETICAL MODEL

The high harmonic spectrum generated from the interaction between the BCCP laser field and Ne atoms is calculated

*zhuxiaosong@hust.edu.cn

by numerically solving the two-dimensional time-dependent Schrödinger equation (TDSE) in length gauge [40,41]. The 2D model potential of Ne atom is given by [42,43] [atomic units (a.u.) are used throughout this paper]

$$V(\vec{r}) = -\frac{Z(\vec{r})}{\sqrt{\vec{r}^2 + a}}, \quad (1)$$

where $Z(\vec{r}) = 1 + 9\exp(-\vec{r}^2)$ and $a = 2.881\,72$ to obtain the ionization potential of Ne atom $I_p = 0.793$ a.u. for $2p$ orbitals. $\vec{r} \equiv (x, y)$ denotes the electron position in the two-dimensional x-y plane.

The bicircular electric field is obtained by combining left-circularly polarized and right-circularly polarized laser fields. The laser vector in the x-y polarized plane is defined by [7]

$$\begin{aligned} E(t) = {} & E_0 f(t)(\cos[\omega t] + \cos[\gamma\omega t])\hat{x} \\ & + E_0 f(t)(\sin[\omega t] - \sin[\gamma\omega t])\hat{y}, \end{aligned} \quad (2)$$

where γ denotes the integer multiple of the fundamental frequency. The laser field has $\gamma + 1$ laser lobes and reflects $\gamma + 1$ fold symmetry. The ω field with helicity $+1$ rotates counterclockwise while the second field $\gamma\omega$ with helicity -1 rotates clockwise. $f(t)$ is the trapezoidal envelop with 2 cycle rising and 2 cycle falling edges and 5 cycle plateau (in units of fundamental). We set the same laser intensity between the ω field and the $\gamma\omega$ field. E_0 is the amplitude of the laser field.

We use the split-operator method to solve the TDSE. To avoid spurious reflections from the spatial boundaries, the electron wave function $\Psi(\vec{r}, t)$ is multiplied by a "mask function" g with the following form [44]:

$$g = g(x)g(y), \quad (3)$$

at each time step, in which

$$g(x) = \begin{cases} 1 & |x| < R_x - L_x \\ \sin^{1/8}\left(\frac{R_x - |x|}{2\pi L_x}\right) & |x| \geqslant R_x - L_x, \end{cases} \quad (4)$$

and

$$g(y) = \begin{cases} 1 & |y| < R_y - L_y \\ \sin^{1/8}\left(\frac{R_y - |y|}{2\pi L_y}\right) & |y| \geqslant R_y - L_y. \end{cases} \quad (5)$$

For all results reported here, we set the width of the "absorbing" area as $L_x = 60$ a.u. and $L_y = 60$ a.u.. In our calculation, we set the range of the "mask function" from -240 a.u. to 240 a.u. in the Cartesian coordinates, i.e., $R_x = R_y = 240$ a.u.. The space step is 0.1 a.u.. The time step is $\Delta t = 0.05$ a.u..

The time-dependent dipole acceleration can be obtained by means of the Ehrenfest theorem,

$$A_q(t) = -\langle\Psi(t)|\frac{\partial}{\partial\vec{r}}V(\vec{r}) - \vec{E}(t)|\Psi(t)\rangle, \quad q = x, y. \quad (6)$$

Then, the harmonic spectrum is obtained by Fourier transforming the dipole acceleration,

$$a_q(\omega) = \int A_q(t)\exp(-iq\omega t)dt. \quad (7)$$

The intensity of left- and right-polarized harmonic components can be obtained by

$$D_{\pm} = |a_{\pm}|^2, \quad (8)$$

where $a_{\pm} = \frac{1}{\sqrt{2}}(a_x \pm ia_y)$. The polarization state of high harmonics can be characterized by the degree of circular polarization (DCP) [32,45–48],

$$\zeta = \frac{D_+ - D_-}{D_+ + D_-}, \quad (9)$$

which can be obtained from the intensity measurements. The ellipticity ϵ has a one-to-one correspondence with the DCP as $\zeta = \frac{2\epsilon}{1+\epsilon^2}$ [22]. The two parameters both vary in the interval from -1 to 1 and have the same sign.

The rotation direction of the electric field can be quantitatively described by the helicity, which is defined as

$$h = \mathrm{sgn}(\epsilon) = \mathrm{sgn}(\zeta). \quad (10)$$

The helicity h takes the values -1 and $+1$, indicating the two opposite rotation directions.

III. RESULTS AND DISCUSSIONS

First, we present the harmonic intensity and the DCP as a function of the harmonic order with different laser parameters in Fig. 1. We choose the example of Ne atoms with the $2p$ ground state. In this case, the two components of the bicircular field with $\gamma = 2$ have equal intensities. According to $a_{\pm} = \frac{1}{\sqrt{2}}(a_x \pm ia_y)$, we transformed the x and y components of dipole acceleration into left- and right-circularly polarized components. Then we, respectively, calculated the intensities of the harmonics with left- and right-circular polarization according to Eq. (8). The harmonic spectra for left-circularly polarized harmonics and right-circularly polarized harmonics are presented with light red lines and blue lines, respectively. Note that, based on the selection rules, the harmonic orders of the left-circularly polarized harmonics are (3n+1) and the harmonic orders of the right-circularly polarized harmonics are (3n−1) [26,31]. One can clearly see this correspondence between the leftand right harmonic component and the orders $(3n + 1/3n − 1)$ in the insets in Figs. 1(a)–1(d). In order to much clearly show the relative intensity between left-circularly polarized harmonics (3n+1) and right-circularly polarized harmonics (3n−1), the envelopes of these harmonic spectra are presented with the dark red solid lines and blue dashed lines correspondingly. One can easily identify the relative intensity between (3n+1)th-order harmonics and the (3n−1)th-order harmonics from the relative height between the two lines. For equal intensities of the two laser field components, the position of the harmonic cutoff is obtained by [22]

$$n\omega = \frac{3.17U_p}{\sqrt{2}} + 1.2|I_p|. \quad (11)$$

The ponderomotive energy of the entire field is defined by $U_p = \frac{2E_0^2}{4\omega^2} + \frac{2E_0^2}{4(2\omega)^2} = U_{p1} + U_{p2}$. The cutoff obtained by Eq. (11) is almost coincident with that from the simulated results.

The harmonic spectrum driven by the bicircular laser field with the fundamental laser wavelength $\lambda_1 = 1300$ nm and laser intensity $I_1 = 1.0 \times 10^{14}$ W/cm^2 is shown in Fig. 1(a). The intensity of the left-circularly polarized harmonics with $h = +1$ ((3n+1)ω) are different from that of the right-circularly polarized harmonics with $h = -1$ ((3n−1)ω). There
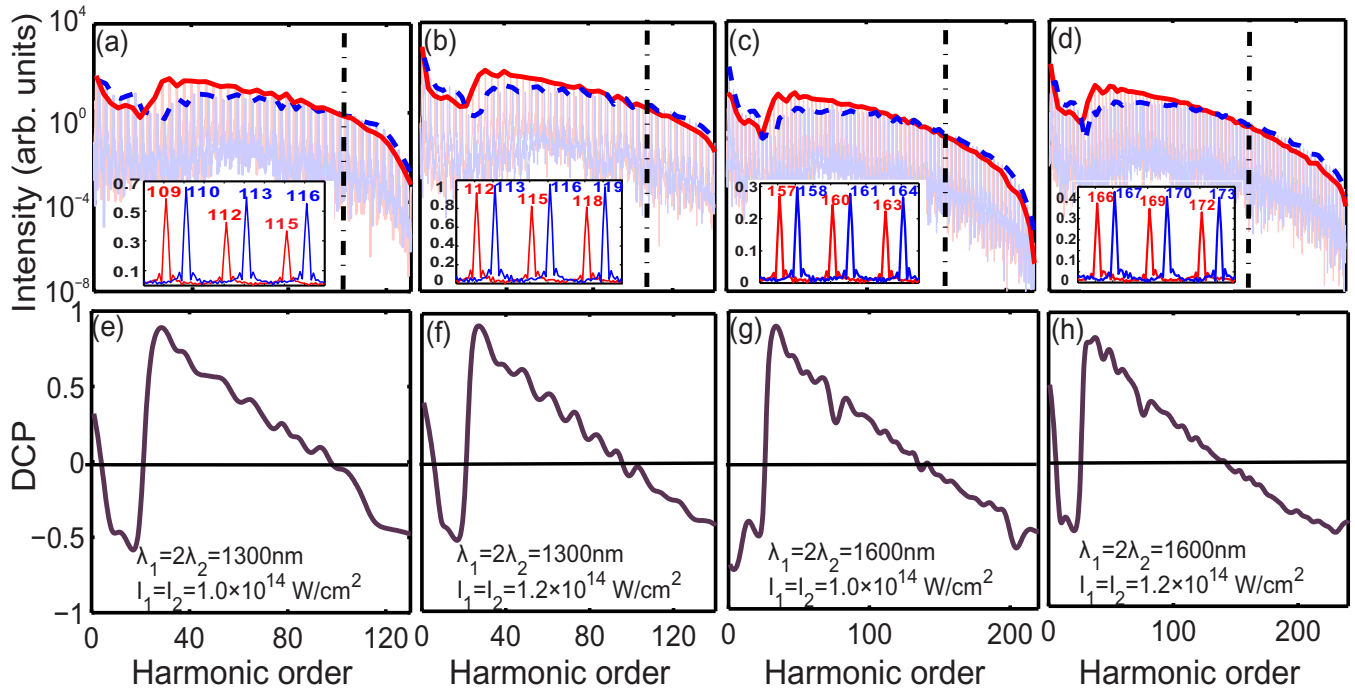
FIG. 1. (a)–(d) Harmonic intensity (e)–(f) DCP as a function of the harmonic order for HHG from the $2p$ orbital of Ne atoms driven by bicircular $\omega - 2\omega$ laser field with different laser parameters. The insets in (a)–(d) show the details of part of harmonic spectra. The left- and right-circularly polarized harmonics are presented as the fine red and blue lines in the insets. The red and blue numbers are the harmonic orders of the left- and right-circularly polarized harmonics. The fundamental laser wavelengths and the laser intensities are (a) and (e) $\lambda_1 = 1300$ nm and $I_1 = I_2 = 1.0 \times 10^{14}$ W/cm^2, (b) and (f) $\lambda_1 = 1300$ nm and $I_1 = I_2 = 1.2 \times 10^{14}$ W/cm^2, (c) and (g) $\lambda_1 = 1600$ nm and $I_1 = I_2 = 1.0 \times 10^{14}$ W/cm^2, (d) and (h) $\lambda_1 = 1600$ nm and $I_1 = I_2 = 1.2 \times 10^{14}$ W/cm^2. The spectra with left- and right-circular polarization are shown as the light red and blue lines, respectively. The envelopes of these harmonic spectra are presented as the dark solid red and blue dashed lines correspondingly.

are two obvious helicity reversions where the red-solid and blue-dashed lines intersect. One is at the ionization threshold (22nd-order harmonic) and the other is at about 107th-order harmonic (labeled by the dash-dot line). Below the ionization threshold, the intensities of (3n+1)th-order harmonics are higher than those of (3n−1)th order. Between the ionization threshold 22nd order and the 107th-order harmonic, the intensities of (3n−1)th-order harmonics turn to be higher than those of the (3n+1)th order. While between 107th-order and the cutoff 120th order obtained by Eq. (11), an opposite result to that between the ionization threshold 22nd order and the 107th-order harmonic order appears. That is, the intensities of the harmonics (3n+1)th order co-rotating with the ω field are higher than those of the (3n−1)th order counter-rotating with the ω field. In order to clearly show the helicity reversion phenomenon in the harmonic spectra, we display the DCP in Fig. 1(e). According to the helicity definition, the helicity reversion appears at the position where the DCP changes its sign. From Fig. 1(e), the DCP crosses zero at the ionization threshold 22nd order and 107th-order harmonic, which is coincident with the discussion above. Besides, for a closer look at the DCP line, an additional helicity reversion is found at the second harmonic order, which will be discussed later.

To check whether the phenomenon is general for the bicircular field interaction with Ne atoms and uncover the reason for the reversion, we apply different laser parameters

for fundamental laser wavelength $\lambda_1 = 1300$ nm, 1600 nm and laser intensity $I_1 = 1.0 \times 10^{14}$ W/cm^2, 1.2×10^{14} W/cm^2. The harmonic spectra are presented in Figs. 1(b)–1(d) and the DCP are plotted in Figs. 1(f)–1(h). It is shown that the intensities of (3n+1)th-order harmonics are higher than those of the (3n−1)th-order harmonics below the ionization threshold, and correspondingly, the values of the DCP are negative. There is a helicity reversion at the ionization threshold for different laser parameters. We have also calculated the harmonic spectra for other model atoms with different two-dimensional soft-core potentials and different ionization potentials. It is shown that the reversion at the threshold is not a general phenomenon and is dependent on the target chosen. From the DCP lines, other helicity reversions are found at the second order below the threshold in Figs. 1(e), 1(f), and 1(h) for a closer look. The first two order harmonics contain the information of the linear response to the two color driving laser field (ω and 2ω). Therefore, the mechanism of these first two harmonics is different from that of other harmonics, and they cannot be simply explained by the HHG process. Besides, the reversions at the second order harmonic in Figs. 1(e), 1(f), and 1(h) are not a regular phenomenon; for instance, it does not appear in Fig. 1(g). They may only happen to appear as a result of the linear response to the laser field. In this work, we focus on the helicity reversions at the above-threshold harmonics, which have close relation to the classical three-step dynamics. The helicity reversion above the threshold is found in all these
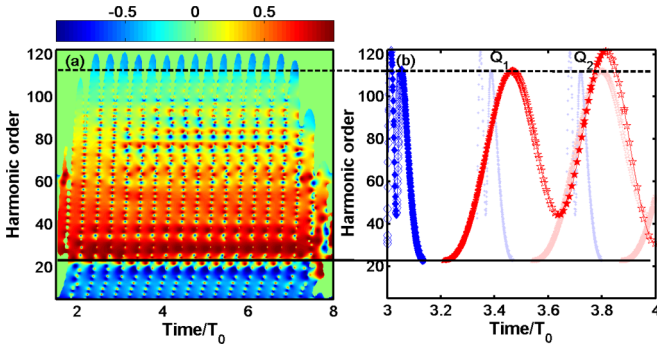
FIG. 2. (a) The time-frequency distribution of the harmonic DCP. (b) The classical paths in the BCCP laser field. The blue diamonds and red pentagrams present the ionization time and the recombination time. The solid markers denote the short trajectories and the hollow markers denote the long trajectories. The laser parameters are the same as in Fig. 1(a). T_0 is the optical cycle of the ω laser field. The horizontal solid line marks the I_p and the dashed line marks the position of the helicity reversion.
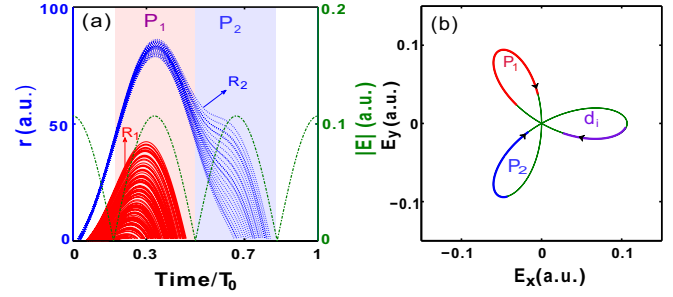

FIG. 3. (a) The amplitude of the electronic field (green dash-dot line, right vertical axis) and the trajectories of the electrons ionized at the first lobe and recombining with the parent ion at the following lobes. The second laser lobe P_1 and the third laser lobe P_2 are superimposed by the light red background and light blue background. The trajectories of the electrons recombining at P_1 are classified as R_1 and presented by red solid lines. The trajectories of the electrons recombining at P_2 are classified as R_2 and presented by blue dotted lines. (b) Laser field vector of the $\omega - 2\omega$ field. Bold purple line d_i represents the electronic field vector at the ionization time at the first laser lobe. Bold red line at P_1 and bold blue line at P_2 represent the electronic laser field vector at the recombination time at the following laser lobes.

spectra. The reversion position is labeled by the dash-dot line in Figs. 1(a)–1(d).

In order to explain the phenomenon of the helicity reversion and elucidate the physics behind it, we present the time-frequency distribution of the harmonic DCP and the classical ionization and recombination paths in Fig. 2. The laser parameters are the same as in Fig. 1(a). Here we analyze the time-frequency properties of the harmonic DCP with the Gabor transform, which has been proved to be a very powerful tool to analyze the emission times of HHG and to clearly discriminate the electron trajectories. Considering the dipole acceleration $A_q(t)$ of Eq. (6), the Gabor transform is defined as [49]

$$GT_q[\Omega, t_0] = \frac{1}{2\pi} \int dt\, A_q(t) e^{-i\Omega t} e^{-(t-t_0)^2/2\sigma^2}, \quad (12)$$

where Ω is the frequency of the high harmonics. In our study, we use $\sigma = 1/3\omega$. The DCP distribution is obtained by $\zeta = \frac{|GT_+|^2 - |GT_-|^2}{|GT_+|^2 + |GT_-|^2}$, in which $GT_\pm = \sqrt{\frac{1}{2}}(GT_x \pm iGT_y)$. In Fig. 2(a), we present the DCP distribution of harmonics between 1.5 optical cycle and 8 optical cycle. Due to the symmetry of the BCCP laser pulse, three radiation bursts per fundamental laser pulse cycle can be found in this figure, as predicted in previous works [7,23–25]. There are two helicity reversions (labeled by the solid line and the dashed line, respectively) and three distinct regions can be identified: (I) Below threshold 22nd order (labeled by the solid line), the DCP is mostly negative. The harmonic emissions counter-rotating with the ω laser field are radiated. (II) The middle region between the threshold (22nd order) and the second reversion (about 107th order, labeled by the dashed line), the DCP is high and positive. The harmonic emissions are emitted with the left-circular polarization. (III) The upper region between the second reversion (about 107th order) and the cutoff (120th order), the DCP is almost negative opposed to the second region. In the second region, the highest DCP is at about the 30th-order harmonic, corresponding to the position of the maximum intensity difference between the left-circularly and

right-circularly polarized harmonic components in Fig. 1(a). Then the pulse DCP decreases gradually along with the increase of the harmonic order. At about 107th order denoted by the dashed line, the DCP transits from positive value to negative value. These are directly reflected in Fig. 1(e).

To give a clear interpretation of the quantum results above, we explore the classical behavior of the electron path by solving Newton's equation under the BCCP laser field driven [50–54]. In Fig. 2(b), we present the electrons classical ionization times labeled by the blue diamonds, as well as the recombination times labeled by the red pentagrams. The solid markers are used for the short trajectories and the hollow markers are used for the long trajectories. Note that HHG in bicircular fields is dominated by short trajectories [22]. We focus on the short trajectories of the electrons ionized at one laser field lobe. As shown in this figure, three ionization bursts and three recombination bursts in one fundamental laser cycle reflect the threefold symmetry of the $\omega - 2\omega$ counter-rotating circularly polarized laser field [20–22]. The electrons ionized in one laser lobe can recombine with the parent ion in the following two lobes and two peaks marked as Q_1 and Q_2 are generated, respectively, at laser lobe P_1 and P_2 [see Fig. 3(b)]. The maxima of the peak Q_1 and peak Q_2 are 111th-order and 122nd-order harmonics, respectively, which approximately correspond to the reversion position and the cutoff position. The slight deviation between the quantum and classical models originates from the quantum effect and the absence of harmonic $3n\omega$ in the quantum model. But it does not influence greatly our conclusion. By comparing the time-frequency analysis and the classical calculations, one can see that the DCP between the ionization threshold and about 40th-order harmonic is positive, which is only contributed by Q_1. However, between the maximum of Q_1 and the harmonic cutoff, the DCP contributed by only Q_2 is negative. Besides, at the overlapping part of the two peaks Q_1 and Q_2 (40th-order

harmonic to 111th-order harmonic), the DCP decreases along with the increase of harmonic order. The correspondence relationship between the time-frequency analysis and the classical calculations indicates that the harmonics generated by Q_1 are left-circularly polarized while the harmonics generated by Q_2 are right-circularly polarized. Therefore, the harmonics, which are contributed by the electrons ionized at one field lobe and recombining at the following adjacent lobes, have opposite helicities.

To further illustrate our idea, we present the electron classical trajectories and the plot of the laser field vector of the $\omega - 2\omega$ field in Fig. 3. The dash-dot green line in Fig. 3(a) is the amplitude of the laser field with three peaks per optical cycle. Every peak corresponds to one laser lobe. In order to increase the readability of the figure, the second lobe marked as P_1 and the third lobe marked as P_2 are superimposed by the light red background and light blue background, respectively. We calculate the short trajectories of the electrons ionized at the first laser lobe. It is found that these trajectories can be classified by the laser lobe they recombine at. That is, the trajectories of the electrons recombining at P_1 are classified as group R_1 (the red lines), and the trajectories of the electrons recombining at P_2 are classified as group R_2 (the blue dot lines). To give a clear description of the trajectory characteristics, the polar plot of the electric field vector of the $\omega - 2\omega$ field is shown in Fig. 3(b). A clover-leaf structure that has a threefold symmetry is presented. The laser field symmetry is reflected by an attosecond pulse train with three pulses generated in one optical cycle in Fig. 2. The electronic field vector at the ionization time at the first laser lobe is marked as the bold purple line d_i. The bold red line at P_1 and the bold blue line at P_2 denote the laser field vector at the recombination times for electrons of groups R_1 and R_2, respectively. The electrons ionized at d_i can recombine with the nucleus at P_1 and P_2 through the path R_1 and R_2. Note that the trajectories R_1 and R_2 correspondingly contribute to short trajectories of Q_1 and Q_2 in Fig. 2(b). Then, based on the discussion about Fig. 2, the harmonics radiated from P_1 and P_2 have opposite helicities.

Next, we also calculate the relative phase of the x, y harmonic components using the strong-field approximation (SFA) model [55,56]. Figures 4(a) and 4(b), respectively, exhibit the calculation results of the harmonic emissions generated by electrons recombining at P_1 and P_2. Based on the classical calculations in Fig. 2(b), we choose the recombination time period and integral over an ionized time period for each recombination time chosen. From this figure, one can see that the relative phase of the two components radiated at the laser lobe P_1 varies between 0.4π and π, which indicates that the radiated harmonics have the positive DCP. However, the relative phase of the two components radiated at the lobe P_2 changes from 0 to -0.5π which indicates that the harmonics have the negative DCP. The result of Fig. 4 coincides with that of Fig. 2. Therefore, our conclusion that the harmonics contributed by electrons ionized at the first lobe and recombining at the following two lobes have opposite helicities is confirmed by using the classical model and the SFA model.

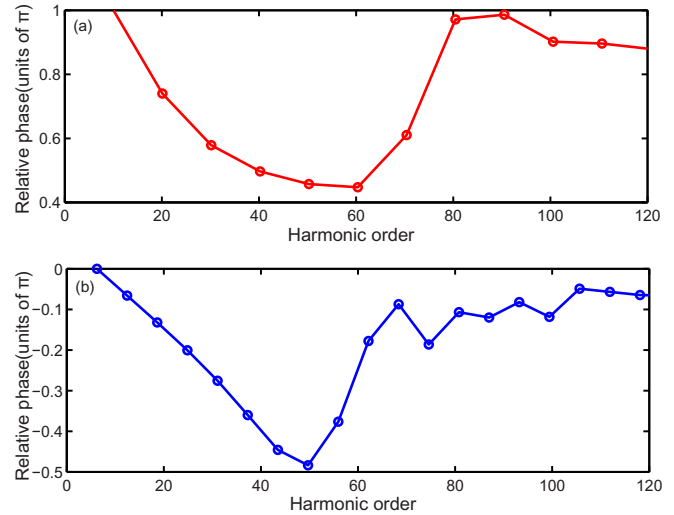Finally, we have also calculated the HHG driven by the BCCP laser field with $\gamma = 3$. The fundamental laser

FIG. 4. The relative phase of the x, y harmonic components radiated from (a) group R_1 and (b) group R_2 as the function of harmonic order.

wavelength and laser intensity are $\lambda_1 = 1300$ nm and $I_1 = 1.0 \times 10^{14}$ W/cm^2, respectively. In Fig. 5(a), the harmonic spectra for left-circularly polarized harmonics $(4n+1)\omega$ and right-circularly polarized harmonics $(4n-1)\omega$ are presented with light red and blue lines, respectively. The envelopes of these harmonic spectra are presented with the dark red solid lines and blue dashed lines correspondingly. In this spectrum, four helicity reversions are obviously observed. The first one is also at the ionization threshold, which is determined by the target. The remaining three reversions are at about 69th order (the dashed line), 80th order, and 95th order (the dash-dot line). In order to clearly display the phenomenon of helicity reversion of the harmonics, we plot the time-frequency distribution of the harmonic DCP. Four attosecond pulses are generated per optical cycle, which reflects the fourfold symmetry of the $\omega - 3\omega$ laser field. The helicity reversions at about 69th order and 95th order are labeled by the dashed line and the dash-dot line. Similarly, the classical electron paths in one optical cycle are exhibited in Fig. 5(c). We only study the trajectories of the electrons ionized at one laser lobe and recombining at the following three lobes. The recombination times of these electrons are labeled by the dark red pentagrams. Others are labeled by the light red pentagrams. Three peaks Q_1, Q_2, and Q_3 are presented in Fig. 5(c). Comparing Fig. 5(b) with Fig. 5(c), it is shown that, the DCP in the region between the ionization threshold 22nd order and the reversion position 69th order is positive and decreases with harmonic order. This region is dominated by Q_1. The region between the reversion position 95th order (the maximum of peak Q_3) and the harmonic cutoff 109th order (the maximum of peak Q_2) is only contributed by Q_2. The helicity of Q_2 is negative, which is opposite to that of Q_1. The helicity reversions at the 69th order and the 95th order in Figs. 5(a) and 5(b) appear at the maxima of Q_1 and Q_3 in Fig. 5(c). In the overlapping region of Q_2 and Q_3 between 69th order and 95th order, the harmonic emissions have both positive and negative DCP and an additional helicity reversion appears. This will be discussed
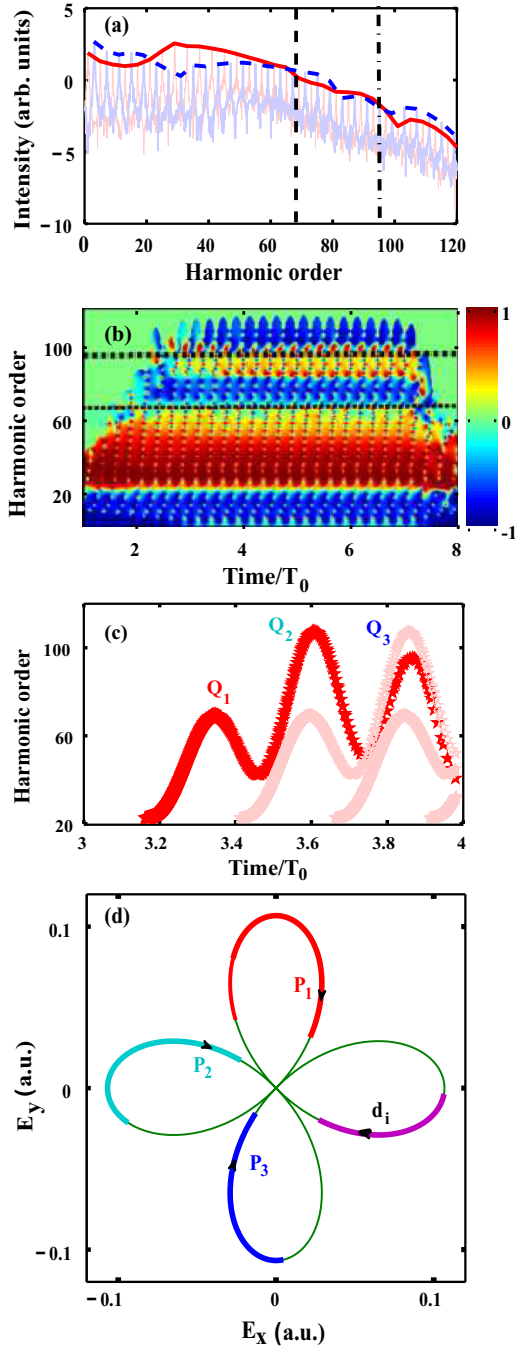
FIG. 5. (a) Harmonic intensity as a function of the harmonic order. The spectra for harmonics co-rotating and counter-rotating with the fundamental field are shown as the light red and blue lines, respectively. The envelopes of these harmonics are presented as the dark solid red and blue dashed lines correspondingly. (b) The time-frequency distribution of the harmonic DCP. (c) The classical recombination paths in the BCCP laser field. (d) The laser field vector of the $\omega - 3\omega$ counter-rotating circularly polarized laser field on the polarization plane. The laser parameters adopted here are $\lambda_1 = 1300$ nm, $I_1 = 1.0 \times 10^{14}$ W/cm^2, $\gamma = 3$.

later. For a clear analysis of the classical electron trajectories in the $\omega - 3\omega$ laser field, the laser field vector is plotted in Fig. 5(d). The electronic field vector at the ionization time at the first laser lobe is marked as the bold purple line d_i. The
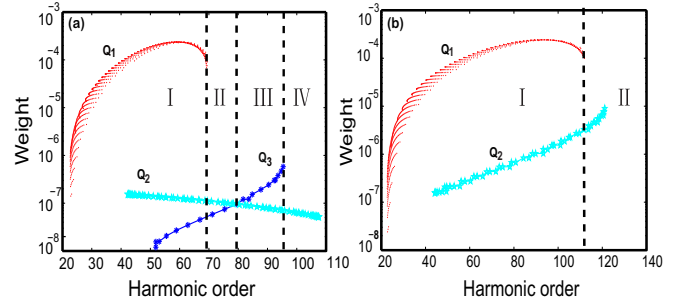

FIG. 6. Weights of the contributing short trajectories in the (a) $\omega - 3\omega$ and (b) $\omega - 2\omega$ BCCP laser fields. The red dots, cyan pentagrams present the weights for peaks Q_1, Q_2 for $\omega - 3\omega$ and $\omega - 2\omega$ laser fields, and the blue stars present the weights for peak Q_3 for the $\omega - 3\omega$ laser field.

recombination times of the short trajectories of Q_1, Q_2, and Q_3 are marked as the red bold line in laser lobe P_1, the cyan bold line in lobe P_2, and the blue bold line in lobe P_3, respectively. It is found that the peaks Q_1, Q_2, and Q_3 are contributed by the electrons recombining at different laser lobes. Based on the above comparison between Figs. 5(b) and 5(c), the harmonic emissions generated in P_1 have opposite helicities with those in P_2, and the helicities of harmonics generated in P_2 are opposite to those in P_3, which is consistent with the conclusion discussed above for the $\omega - 2\omega$ laser field.

To understand the appearance of the additional helicity reversal in the overlapping region of Q_2 and Q_3, the weights of the contributing electron trajectories should be obtained. Figure 6 shows the weights of the short trajectories in both the $\omega - 3\omega$ and $\omega - 2\omega$ laser fields. For each trajectory, the weight is calculated by $W(t_0, v_\perp) = W_0(t_0) W_1(v_\perp)$. $W_0(t_0)$ is the ionization rate at time t_0 obtained from the TDSE simulation by calculating the derivative of the time-dependent ionization probability. $W_1(v_\perp)$ is the weight with a Gaussian distribution for the tunnel electron with transverse initial velocity $v_\perp$ [57]. For the $\omega - 3\omega$ laser field as shown in Fig. 6(a), the spectrum range can be divided into four regions. In the first region below the 69th order, the weight of peak Q_1 is much greater than those of peaks Q_2 and Q_3. In the second region from the 69th order to the 79th order, peak Q_1 disappears and the weight of Q_2 is greater than Q_3. Then from about 79th order to 95th order, the weight of Q_3 becomes greater than Q_2 in the third region. In the last region above the 95th order, only peak Q_2 remains contributing to the harmonic emissions. In each region, the helicity of the generated harmonics is determined by helicity of the strongest contributing peak, which can well explain the results in Figs. 5(a) and 5(b). Owing to the intersection between the weights of peaks Q_2 and Q_3, the additional helicity reversal in the overlapping region of Q_2 and Q_3 appears. For the $\omega - 2\omega$ laser field as shown in Fig. 6(b), the spectrum range can be divided by the 111th order into two regions. The weight of peak Q_1 is much greater than that of peak Q_2 in the first region. In the second region, only peak Q_2 contributes to the harmonic emissions. Since the weights of the two peaks have no intersection, there is no extra helicity reversal in the $\omega - 2\omega$ BCCP laser field.

Based on all the discussions above, a picture of the electron classical trajectories in HHG driven by BCCP laser

field is revealed. Besides, the correspondence between the harmonic polarization and the classical trajectories has also been established. Specifically, the electron ionized at one laser lobe can recombine with the nucleus at the following laser lobes. These recombining trajectories can be classified into different groups based on the laser lobe they are recombining at. Moreover, the harmonics emitted from these groups at adjacent laser lobes have opposite helicities. For instance, in the $\omega - 2\omega$ laser field, groups R_1 and R_2 are both ionized at one laser lobe d_i. And they recombine with the nucleus at the following laser lobes P_1 and P_2 and form the peaks Q_1 and Q_2, respectively. The harmonics from Q_1 and Q_2 are radiated with opposite helicities and the helicity reversion occurs at the maximum of Q_1. In the $\omega - 3\omega$ laser field, electrons ionized at one laser lobe d_i recombine at the following lobes P_1, P_2, P_3 and form the peaks Q_1, Q_2, Q_3, respectively. The harmonics from peaks Q_1 and Q_3 have positive helicity while those from Q_2 have negative helicity. The helicity reversion occurs at the position where the dominantly contributing peak is changed to its neighboring peak, i.e., at the maxima of Q_1 and Q_2 and at the intersection between the weights of Q_2 and Q_3.

IV. CONCLUSION

In conclusion, under the interaction of bicircular laser field with the 2D model Ne atoms, a harmonic spectrum with different helicities in different spectrum ranges is generated. It is shown that the helicity of the elliptically polarized harmonic emission is reversed at particular harmonic orders. Based on the time-frequency analysis and the classical three-step model, the relationship between the reversion position and the electron trajectories is obtained. The electrons ionized at one lobe of laser field can recombine with the nucleus at the following laser lobes radiating harmonics. These harmonic emissions generated from adjacent laser lobes have opposite helicities. Besides, we confirm our conclusion through the calculation of relative phase by the SFA model. Our study performs a detailed analysis for the HHG driven by the BCCP laser field in terms of the classical trajectories and established the correspondence between the harmonic polarization and the classical trajectories.

[1] P. B. Corkum and F. Krausz, Nat. Phys. **3**, 381 (2007).

[2] F. Krausz and M. Ivanov, Rev. Mod. Phys. **81**, 163 (2009).

[3] X. Zhu, X. Liu, Y. Li, M. Qin, Q. Zhang, P. Lan, and P. Lu, Phys. Rev. A **91**, 043418 (2015).

[4] L. He, P. Lan, Q. Zhang, C. Zhai, F. Wang, W. Shi, and P. Lu, Phys. Rev. A **92**, 043403 (2015).

[5] X. Zhu, M. Qin, Q. Zhang, W. Hong, Z. Xu, and P. Lu, Opt. Express **20**, 16275 (2012).

[6] G. Sansone, E. Benedetti, F. Calegari, C. Vozzi, L. Avaldi, R. Flammini, L. Poletto, P. Villoresi, C. Altucci, R. Velotta, S. Stagira, S. de silvestri, and M. Nisoli, Science **314**, 443 (2006).

[7] L. Medišauskas, J. Wragg, H. van der Hart, and M. Y. Ivanov, Phys. Rev. Lett. **115**, 153001 (2015).

[8] A. L. Cavalieri, N. Müller, T. Uphues, V. S. Yakovlev, A. Baltuška, B. Horvath, B. Schmidt, L. Blümel, R. Holzwarth, S. Hendel, M. Drescher, U. Kleineberg, P. M. Echenique, R. Kienberger, F. Krausz, and U. Heinzmann, Nature (London) **449**, 1029 (2007).

[9] J. Itatani, J. Levesque, D. Zeidler, H. Niikura, H. Pépin, J. C. Kieffer, P. B. Corkum, and D. M. Villeneuve, Nature (London) **432**, 867 (2004).

[10] S. Haessler, J. Caillat, W. Boutu, C. Giovanetti-Teixeira, T. Ruchon, T. Auguste, Z. Diveki, P. Breger, A. Maquet, B. Carré, R. Taïeb, and P. Salières, Nat. Phys. **6**, 200 (2010).

[11] P. M. Kraus *et al.*, Science **350**, 790 (2015).

[12] C. Zhai, L. He, P. Lan, X. Zhu, Y. Li, F. Wang, W. Shi, Q. Zhang, and P. Lu, Scientific Reports **6**, 23236 (2016); M. Qin and X. Zhu, Opt. Laser Technol. **87**, 79 (2017).

[13] O. Smirnova, Y. Mairesse, S. Patchkovskii, N. Dudovich, D. Villeneuve, P. Corkum, and M. Y. Ivanov, Nature (London) **460**, 972 (2009).

[14] S. Baker, J. Robinson, C. Haworth, H. Teng, R. A. Smith, C. C. Chirilă, M. Lein, J. W. G. Tisch, and J. P. Marangos, Science **312**, 424 (2006).

[15] H. J. Wörner, J. B. Bertrand, D. V. Kartashov, P. B. Corkum, and D. M. Villeneuve, Nature (London) **466**, 604 (2010).

[16] O. Travnikova, J.-C. Liu, A. Lindblad, C. Nicolas, J. Söderström, V. Kimberg, F. Gelmukhanov, and C. Miron, Phys. Rev. Lett. **105**, 233001 (2010).

[17] C. Boeglin, E. Beaurepaire, V. Halt, V. López-Flores, C. Stamm, N. Pontius, H. A. Dürr, and J.-Y. Bigot, Nature (London) **465**, 458 (2010).

[18] P. B. Corkum, Phys. Rev. Lett. **71**, 1994 (1993).

[19] K. J. Schafer, B. Yang, L. F. DiMauro, and K. C. Kulander, Phys. Rev. Lett. **70**, 1599 (1993).

[20] S. Long, W. Becker, and J. K. McIver, Phys. Rev. A **52**, 2262 (1995).

[21] H. Eichmann, A. Egbert, S. Nolte, C. Momma, B. Wellegehausen, W. Becker, S. Long, and J. K. McIver, Phys. Rev. A **51**, R3414 (1995).

[22] D. B. Milošević, W. Becker, and R. Kopold, Phys. Rev. A **61**, 063403 (2000).

[23] D. B. Milošević, Opt. Lett. **40**, 2381 (2015).

[24] D. B. Milošević, Phys. Rev. A **92**, 043827 (2015).

[25] D. B. Milošević and W. Becker, Phys. Rev. A **62**, 011403 (2000).

[26] A. Fleischer, O. Kfir, T. Diskin, P. Sidorenko, and O. Cohen, Nat. Photonics **8**, 543 (2014).

[27] O. Kfir, P. Grychtol, E. Turgut, R. Knut, D. Zusin, D. Popmintchev, T. Popmintchev, H. Nembach, J. M. Shaw, A. Fleischer, H. Kapteyn, M. Murnane, and O. Cohen, Nat. Photonics **9**, 99 (2015).

[28] D. M. Reich and L. B. Madsen, Phys. Rev. A **93**, 043411 (2016).

[29] A. Ferré, C. Handschin, M. Dumergue, F. Burgy, A. Comby, D. Descamps, B. Fabre, G. A. Garcia, R. Géneaux, L. Merceron, E. Mével, L. Nahon, S. Petit, B. Pons, D. Staedter, S. Weber, T. Ruchon, V. Blanchet, and Y. Mairesse, Nat. Photonics **9**, 93 (2014).

[30] O. E. Alon, V. Averbukh, and N. Moiseyev, Phys. Rev. Lett. **80**, 3743 (1998).

[31] E. Pisanty, S. Sukiasyan, and M. Ivanov, Phys. Rev. A **90**, 043829 (2014).

[32] D. B. Milošević, J. Phys. B **48**, 171001 (2015).

[33] F. Mauger, A. D. Bandrauk and T. Uzer, J. Phys. B **49**, 10LT01 (2016).

[34] D. D. Hickstein, F. J. Dollar, P. Grychtol, J. L. Ellis, R. Knut, C. Hernández-García, D. Zusin, C. Gentry, J. M. Shaw, T. Fan, K. M. Dorney, A. Becker, A. Jaroń-Becker, H. C. Kapteyn, M. M. Murnane, and C. G. Durfee, Nat. Photonics **9**, 743 (2015).

[35] U. Hergenhahn, E. E. Rennie, O. Kugeler, S. Marburger, T. Lischke, I. Powis, and G. Garcia, J. Chem. Phys. **120**, 4553 (2004).

[36] N. Böwering, T. Lischke, B. Schmidtke, N. Müller, T. Khalil, and U. Heinzmann, Phys. Rev. Lett. **86**, 1187 (2001).

[37] I. Powis, J. Chem. Phys. **112**, 301 (2000).

[38] D. Baykusheva, M. S. Ahsan, N. Lin, and H. J. Wörner, Phys. Rev. Lett. **116**, 123001 (2016).

[39] D. M. Reich and L. B. Madsen, Phys. Rev. Lett. **117**, 133902 (2016).

[40] M. D. Feit, J. A. Fleck, Jr., and A. Steiger, J. Comput. Phys. **47**, 412 (1982).

[41] M. He, Y. Li, Y. Zhou, M. Li, and P. Lu, Phys. Rev. A **93**, 033406 (2016).

[42] I. Barth and M. Lein, J. Phys. B **47**, 204016 (2014).

[43] X. Zhu, P. Lan, K. Liu, Y. Li, X. Liu, Q. Zhang, I. Barth, and P. Lu, Opt. Express **24**, 4196 (2016).

[44] K. J. Yuan and A. D. Bandrauk, Phys. Rev. A **83**, 063422 (2011).

[45] P. Antoine, B. Carre, A. L'Huillier, and M. Lewenstein, Phys. Rev. A **55**, 1314 (1997).

[46] E. Hecht, *Optics*, 4th ed. (Pearson Education, Essex, 2014).

[47] M. Born and E. Wolf, *Principles of Optics* (Pergamon Press, Oxford, 1970).

[48] S. Odžak and D. B. Milošević, Phys. Rev. A **92**, 053416 (2015).

[49] C. C. Chirilă, I. Dreissigacker, E. V. van der Zwan, and M. Lein, Phys. Rev. A **81**, 033412 (2010).

[50] X. Ma, Y. Zhou, and P. Lu, Phys. Rev. A **93**, 013425 (2016).

[51] Z. Wang, M. Li, Y. Zhou, Y. Li, P. Lan, and P. Lu, Phys. Rev. A **93**, 013418 (2016).

[52] Y. Chen, Y. Zhou, Y. Li, M. Li, P. Lan, and P. Lu, J. Chem. Phys. **144**, 024304 (2016).

[53] A. Tong, Y. Zhou, and P. Lu, Opt. Express **23**, 15774 (2015).

[54] M. Li, P. Zhang, S. Luo, Y. Zhou, Q. Zhang, P. Lan, and P. Lu, Phys. Rev. A **92**, 063404 (2015).

[55] Y. Zhou, O. I. Tolstikhin, and T. Morishita, Phys. Rev. Lett. **116**, 173001 (2016).

[56] M. Lewenstein, Ph. Balcou, M. Yu. Ivanov, A. L'Huillier, and P. B. Corkum, Phys. Rev. A **49**, 2117 (1994).

[57] N. B. Delone and V. P. Krainov, J. Opt. Soc. Am. B **8**, 1207 (1991).